

Formation of magnetic discontinuities through superposition of force-free magnetic fields: Periodic boundaries

Dinesh Kumar¹, R. Bhattacharyya¹, and P. K. Smolarkiewicz²

¹ *Udaipur Solar Observatory, Physical Research Laboratory,
Dewali, Bari Road, Udaipur-313001, India and*

² *European Centre for Medium-Range Weather Forecasts, Reading RG2 9AX, UK.*

(Dated: October 15, 2013)

Abstract

In ideal magnetohydrodynamics characterized by an infinite electrical conductivity, the magnetic flux across an arbitrary fluid surface is conserved in time. The magnetofluid then can be partitioned into contiguous subvolumes of fluid, each of which entraps its own subsystem of magnetic flux. During dynamical evolution of the magnetofluid these subvolumes press into each other, and in the process two such subvolumes may come into direct contact while ejecting a third interstitial subvolume. Depending on the orientations of magnetic fields of the two interacting subvolumes the magnetic field at the common surface of interaction may become discontinuous and a current sheet is formed there. This process of current sheet formation and their subsequent decay is believed to be a plausible mechanism for coronal heating and may also be responsible for various eruptive phenomena at the solar corona. In this work, we explore this theoretical concept through numerical simulations of a viscous, incompressible magnetofluid characterized by infinite electrical conductivity. In particular, we show that if the initial magnetic field is prescribed by superposition of two linear force-free fields with different torsion coefficients, then formation of current sheets are numerically realizable in the neighborhood of magnetic nulls.

PACS numbers: 52.25.Xz, 52.30.Cv, 52.35.Vd, 95.30.Qd

Keywords: MHD, Current Sheet, EULAG, Solar/Stellar atmosphere

I. INTRODUCTION

An ideal magnetofluid characterized by infinite electrical conductivity evolves with magnetic field lines being tied to fluid parcels—referred as the frozen-in condition or flux freezing. As a consequence, the magnetic flux across an arbitrary fluid surface [1], physically identified by the material elements lying on it, remains conserved in time. However, observed magnetofluids are not ideal but have a small but non-zero electrical diffusivity η . The two limits, diffusive or ideal, of the single-fluid magnetohydrodynamics (MHD) is then determined by the magnetic Reynolds number $R_M = VL/\eta$ in usual notations representing the ratio of nonlinearity to dissipation. The astrophysical magnetofluids satisfies the condition $R_M \gg 1$ globally and hence can be considered as near-ideal systems for all practical purposes. For example, the solar corona with its million degree Kelvin temperature and 10-15 Gauss ambient magnetic field has a Spitzer diffusivity of $\approx 1 \text{ m}^2\text{s}^{-1}$ [2]. Then for a typical length scale $L \approx 10^7\text{m}$, and characteristic speed $V \approx 10^3\text{ms}^{-1}$, $R_M \approx 10^{10}$ which qualifies the solar corona to be a near-ideal magnetofluid where the frozen-in condition is satisfied to a good approximation.

Because of this frozen-in condition, in near-ideal systems a magnetic flux surface everywhere tangential to the magnetic field \mathbf{B} , once identified as a fluid surface will maintain this identity throughout subsequent evolution of the fluid. This equivalence in fluid and flux surfaces enables to partition the magnetofluid into contiguous magnetic subvolumes each entrapping its own magnetic flux system [3]. If two such magnetic subvolumes press into each other and come into direct contact by squeezing out a third interstitial subvolume, then under favorable conditions the magnetic field is expected to get discontinuous across their common surface of interaction [1]. For such a discontinuous magnetic field the Ampere's law gives a current density $\mathbf{J} = (c/4\pi)\nabla \times \mathbf{B}$, contained entirely in the plane across which the magnetic field is discontinuous and hence forms a current sheet (CS).

The above possibility of CS formation through pressing of magnetic subvolumes is imminent from the optical analogy of magnetic field lines proposed by Parker [4–7]. Although more general in approach, the analogy in relation to an equilibrium magnetic field is based on the similarity in field line equations of a potential field $\mathbf{B}_p = -\nabla\phi$ on the corresponding flux surface S , with the optical ray paths in a medium with refractive index $|\nabla\phi|$. The magnetic field lines on different S surfaces then stream according to Fermat's principle and

get refracted like optical rays. Further analysis shows this refraction to deflect a field line concavely towards the local maximum in $|\mathbf{B}_p|$. The trajectory of a stream of field lines laying on a given S surface then locally exclude a region of sufficient maximum in $|\mathbf{B}_p|$, resulting in a gap on the flux surface. This gap extends to a hole in a stack of such flux surfaces. In a dynamical scenario, a local compression of two magnetic subvolumes on either sides of this stack then enables corresponding magnetic field lines to intrude through the hole and come into direct contact. These intruding field lines being in general not parallel, a formation of CS is inevitable at the contact.

Albeit stated here in terms of a potential field which is trivially untwisted, the optical analogy is also applicable for a twisted magnetic field [7]. For completeness, here we provide a rationale in favor of this applicability by noting that a twisted magnetic field can be expressed as a superposition of component fields where each component is untwisted [8]. For every component field, magnetic flux surfaces can be constructed by a pair of Euler potentials (EPs) (ξ_i, ζ_j) [9, 10]. The magnetic field is then

$$\mathbf{B} = \sum_j \mathbf{B}_j = \sum_j W_j(\xi_j, \zeta_j) \nabla \xi_j \times \nabla \zeta_j \quad , \quad (1)$$

where the index j specifies a component field with magnitude W_j . Both ξ_j -constant and ζ_j -constant surfaces are then magnetic flux surfaces of the component \mathbf{B}_j . The magnetic field lines being the lines of intersection of the two surfaces, the magnetic topology is then essentially determined by the EPs. The vector field

$$\mathbf{A}'_j = \frac{\mathbf{B}_j}{W(\xi_j, \zeta_j)} = \nabla \xi_j \times \nabla \zeta_j \quad , \quad (2)$$

is then topologically identical to \mathbf{B}_j . The optical analogy is then applicable to the potential field defined as

$$\mathbf{A}_j = \frac{\mathbf{A}''_j}{\xi_j} = \nabla \zeta_j \quad , \quad (3)$$

where the vector $\mathbf{A}''_j = \nabla \times \mathbf{A}'_j$. Noting that a gap in the field lines on a flux surface is a gap on the flux surface itself, holes will be created in stacks of ξ_j -constant and ζ_j -constant surfaces also. The optical analogy is then applicable to each of the component fields with their locally defined flux surfaces. Further the superposition being linear, a formation of CS on any one of the local flux surfaces will result in enhancing the total current density.

In the ideal limit of zero resistivity, the field lines are prohibited to diffuse from one subvolume to the other and the discontinuity in \mathbf{B} achieves its true mathematically singular limit. In a near-ideal magnetofluid however, as the gradient in \mathbf{B} sharpens a threshold is reached where the magnetic Reynolds number becomes locally small because of the decrease in L , the scale over which the magnetic field varies. As a consequence the magnetofluid becomes locally diffusive resulting in magnetic reconnection [11] through which magnetic energy gets converted into heat and kinetic energy. This fundamental heating mechanism is believed to be one of the possible causes to maintain the solar corona at its million degree Kelvin temperature [7].

The analytical demonstration of spontaneous CS formation in a static magnetofluid with infinite electrical conductivity was first proposed by Parker [12, 13] and is recently revisited in reference [14]. The demonstration essentially utilizes the impossibility of satisfying the two stringent conditions of ideal MHD, the local force balance and the conservation of global magnetic topology as a consequence of flux freezing, with an interlaced magnetic field continuous everywhere. The impossibility in simultaneous satisfaction of the above two constraints of ideal MHD can further be explained in terms of the overdetermined nature of magnetostatic partial differential equations nonlinearly coupled to the integral equations imposing the field topology, and the hyperbolic nature of the torsion coefficient α_0 of a force-free equilibrium characterized by zero Lorentz force [15]. It is further demonstrated by Low [16] that the magnetic topologies of the force-free fields obtainable from an uniform magnetic field through continuous deformation by magnetic footpoint displacements at the end plates of Parker's magnetostatic theorem are a restricted subset of the field topologies similarly created without imposing the force-free condition. The theorem then follows by concluding that a continuous nonequilibrium field with a topology not in this subset must relax to a terminal state containing magnetic discontinuities. To focus on ideas, we consider an incompressible, thermally homogeneous, viscous magnetofluid with infinite electrical conductivity bounded in a triply periodic Cartesian domain. The dynamics of the fluid is then governed by the relevant MHD Navier-Stokes equations

$$\rho_0 \left(\frac{\partial \mathbf{v}}{\partial t} + (\mathbf{v} \cdot \nabla) \mathbf{v} \right) = \mu_0 \nabla^2 \mathbf{v} + \frac{1}{4\pi} (\nabla \times \mathbf{B}) \times \mathbf{B} - \nabla p, \quad (4)$$

$$\nabla \cdot \mathbf{v} = 0, \quad (5)$$

$$\frac{\partial \mathbf{B}}{\partial t} = \nabla \times (\mathbf{v} \times \mathbf{B}), \quad (6)$$

$$\nabla \cdot \mathbf{B} = 0, \quad (7)$$

in standard notations, where ρ_0 and μ_0 are uniform density and coefficient of viscosity respectively. Equation (7) is redundant in the sense that it is implied for all time by the induction equation (6) if an initial field is chosen to be solenoidal. If released from an initial nonequilibrium state, the magnetofluid would relax towards a terminal state by converting magnetic energy W_M to kinetic energy W_K through equations

$$\frac{dW_K}{dt} = \int \frac{1}{4\pi} [(\nabla \times \mathbf{B}) \times \mathbf{B}] \cdot \mathbf{v} d^3x - \int \mu_0 |\nabla \times \mathbf{v}|^2 d^3x, \quad (8)$$

$$\frac{dW_M}{dt} = - \int \frac{1}{4\pi} [(\nabla \times \mathbf{B}) \times \mathbf{B}] \cdot \mathbf{v} d^3x, \quad (9)$$

$$\frac{dW_T}{dt} = - \int \mu_0 |\nabla \times \mathbf{v}|^2 d^3x, \quad (10)$$

where the integral is over a full period. The irreversible loss of energy as heat from the system is via viscous dissipation since the Lorentz force is conservative. The terminal relaxed state then has zero velocity and is in magnetostatic equilibrium since the magnetic field cannot decay to zero because of flux freezing. In absence of magnetic diffusivity the magnetic topology of the terminal state is the same as of the initial state. For an initially complex magnetic topology, formation of CSs are then expected as the magnetofluid relaxes to the terminal state— paving a way to understand the dynamics of CS formation through a viscous relaxation. The terminal equilibrium being also a minimum energy state, any resistive diffusion of the developed CSs in a near-ideal magnetofluid would be opposed by the Maxwell stresses. The combined effect is then a general restriction of the thickness of CSs to a value of $\epsilon < L/N^{1/2}$ where $N = (LV_A)/\eta$ is the Lundquist number and V_A is the Alfvén speed [7].

In light of the above discussion, a point to be emphasized is the possible importance of an unbalanced force (Lorentz force + pressure gradient) counterbalancing the viscous drag in a magnetofluid with infinite electrical conductivity. Such systems can be realized depending on the length and time scales of the physical processes involved. For instance, in solar corona the fluid Reynolds number is only $R_F \approx 10$ [2] in comparison to the magnetic Reynolds number of $R_M \approx 10^{10}$. Then the corona can be interpreted as an infinitely conducting but viscous magnetofluid at appropriate intermediate scales lying between the large scales where

nonlinearity dominates and the small scales where magnetic diffusivity is effective. Noting that the frozen-in condition defines a fluid surface to be a valid magnetic flux surface, if two such flux surfaces are pressed into each other then the velocity gradient and the corresponding viscous drag also increases along with the current density. Because of the lower value of fluid Reynolds number, the time scale for viscous diffusion is smaller than the same for magnetic diffusion and the corresponding viscous drag may prevent two magnetic subvolumes from coming into direct contact with each other resulting in prohibition of CS formation. Then a CS is expected to form only in presence of a suitable force that overcomes this viscous drag, which facilitates in bringing the two magnetic subvolumes into direct contact of each other. A proof of concept for the above understanding of CS formation through progressive pressing of magnetic subvolumes has already been demonstrated in a recent numerical experiment [1] where the initial magnetic field is represented in terms of a pair of global magnetic flux surfaces. The intersection curves of these two flux surfaces then represent magnetic field lines. The advantage of the above work is in its advection of magnetic flux surfaces instead of magnetic field, leading to simpler equations along with elimination of possible post processing errors in determining magnetic topology. In addition, the flux surface representation opens up the possibility to analyze results in terms of the optical analogy. An apt trade-off for this advantage is the assumption of the initial magnetic field to be untwisted, since only for such fields global magnetic flux surfaces exist whereas; observations suggest most of the magnetic field relevant to astrophysical plasmas, including the solar corona, to be twisted. A manifestation of this twisted magnetic field lines are sigmoidal structures observed on the photosphere, as explained briefly in reference [3]. In this work, our motivation is to numerically demonstrate CS formation with an initial twisted magnetic field in relevance to general magnetic morphology of the solar corona.

A representation of twisted magnetic field in terms of EPs is difficult since there is no unique way to determine the required number of untwisted components, the number being essentially determined by the mathematical advantage of a given representation [1]. Additionally, choice of a pair of EPs for a given component field is not unique either [9, 10]. A successful numerical simulation for understanding CS formation then requires a judicious breakup of \mathbf{B} in component fields along with selection of EPs that are advantageous for the understanding. Finally the complex dynamics of each local flux surfaces are to be related to the evolution of the total magnetic field and current density to arrive at the complete

picture. In addition, an increase in general complexity of twisted fields may require large number of component fields that increases computational cost manifold. To circumvent these difficulties, here we adapt the more conventional approach of advecting the total magnetic field instead of the local flux surfaces. Nonetheless, a comparison with optical analogy is still possible in our computations, for example the squashing of an X-type neutral point to two Y-type neutral points described latter in the paper.

In a tenuous magnetofluid like the solar corona, the plasma- β ratio of kinetic to magnetic pressure being very small, the only available force to counterbalance the viscous drag is the Lorentz force. Based on this general understanding, in a recent work by Ravindra *et. al* [17] it is demonstrated that if a newly emerged magnetic flux described by a linear force-free equation enters into a region already preoccupied by a different linear force-free field at the coronal height, then the superposed state has a nonzero Lorentz force. It is further conjectured that this unbalanced Lorentz force may be responsible to generate CSs through progressive pressing of magnetic subvolumes. The subsequent magnetic reconnection is then responsible for the observed solar flares. Motivated by the above proposal, here we numerically demonstrate the feasibility of CS formation using an idealized scenario of Direct Numerical Simulation (DNS) in a triply periodic Cartesian domain. The initial magnetic field is assumed to be a superposition of two linear force-free fields which are in general agreement with the twisted coronal magnetic fields, and also mimics a possible scenario of flux emergence as envisioned in reference [17]. In addition, such a superposed magnetic field can also be perceived as a spontaneously achieved two-fluid relaxed state [3].

The paper is organized as follows. The IVPs and the numerical model are discussed in sections II and III respectively while simulation results are presented in section IV. Section V summarizes these results and comments on possible future works.

II. INITIAL VALUE PROBLEM

In this section we develop the initial value problem in terms of two superposed linear force-free fields. The mathematics is fundamentally the same as outlined in the appendix of [17], presented here with more details for completeness. Let \mathbf{B}_1 and \mathbf{B}_2 are two linear force free fields satisfying

$$\nabla \times \mathbf{B}_1 = \alpha_1 \mathbf{B}_1 , \quad (11)$$

$$\nabla \times \mathbf{B}_2 = \alpha_2 \mathbf{B}_2 \quad (12)$$

with torsion coefficients α_1 and α_2 representing the magnetic circulations per unit flux for \mathbf{B}_1 and \mathbf{B}_2 [14] respectively. A overlapped magnetic field is then created by a linear superposition of \mathbf{B}_1 and \mathbf{B}_2 , written as

$$\mathbf{B}' = \mathbf{B}_1 + \gamma \mathbf{B}_2 , \quad (13)$$

where γ is a constant weighing factor related to the amplitudes of the two superposed fields and represents the deviation of \mathbf{B}' from its force-free configuration. The field lines for \mathbf{B}' are also twisted, as can easily be verified by noting $\mathbf{J} \cdot \mathbf{B}' \neq 0$ except for the trivial case of $|\mathbf{B}_1| = |\mathbf{B}_2| = 0$.

The Lorentz force exerted by \mathbf{B}' is then given by

$$\mathbf{J} \times \mathbf{B}' = \frac{1}{\mu} \gamma (\alpha_1 - \alpha_2) \mathbf{B}_1 \times \mathbf{B}_2 . \quad (14)$$

For a triply periodic domain in Cartesian geometry, the components of \mathbf{B}' are

$$\begin{aligned} B'_x = & k_1 k_2 \cos(k_1 x) \cos(k_2 y) \sin(k_3 z) - \alpha_1 k_3 \sin(k_1 x) \\ & \sin(k_2 y) \cos(k_3 z) + \gamma [l_1 l_2 \cos(l_1 x) \cos(l_2 y) \sin(l_3 z) \\ & - \alpha_2 l_3 \sin(l_1 x) \sin(l_2 y) \cos(l_3 z)], \end{aligned} \quad (15)$$

$$\begin{aligned} B'_y = & (k_1^2 + k_3^2) \sin(k_1 x) \sin(k_2 y) \sin(k_3 z) + \gamma [(l_1^2 + l_3^2) \\ & \sin(l_1 x) \sin(l_2 y) \sin(l_3 z)], \end{aligned} \quad (16)$$

$$\begin{aligned} B'_z = & k_2 k_3 \sin(k_1 x) \cos(k_2 y) \cos(k_3 z) + \alpha_1 k_1 \cos(k_1 x) \\ & \sin(k_2 y) \sin(k_3 z) + \gamma [l_2 l_3 \sin(l_1 x) \cos(l_2 y) \cos(l_3 z) \\ & + \alpha_2 l_1 \cos(l_1 x) \sin(l_2 y) \sin(l_3 z)], \end{aligned} \quad (17)$$

with $\alpha_1 = \sqrt{k_1^2 + k_2^2 + k_3^2}$ and $\alpha_2 = \sqrt{l_1^2 + l_2^2 + l_3^2}$; the triplets $k = \{k_1, k_2, k_3\}$ and $l = \{l_1, l_2, l_3\}$ representing different modes. From equation (14) then for conditions $k = l$ or $\gamma = 0$, \mathbf{B}' is force-free. We consider $\mathbf{B}'(x, y, z) = \mathbf{H}(x, y, z)$, characterized by $k = \{1, 1, 1\}$, $l = \{2, 2, 2\}$ and $\gamma = 0.5$, as the initial magnetic field in our simulations.

In the following we describe the magnetic topology of \mathbf{H} in terms of magnetic nulls and separators [18], since CSs are expected to form at the neighborhood of these structures [19]. Also it is to be noted that CS formation in three dimensions can also occur in absence of nulls [20]. Figure 1(a) illustrates all possible nulls of \mathbf{H} in the computational domain of volume $(2\pi)^3$. The illustrations of magnetic nulls in this paper use the condition $\mathbf{B} = 0$ at the null points. For the purpose, we define a Gaussian function

$$\psi(x, y, z) = \exp \left[- \sum_{i=x,y,z} \frac{(H_i(x, y, z) - H_0)^2}{d_0} \right]. \quad (18)$$

where d_0 determines width of the Gaussian and H_0 represents a particular isovalue of H_x, H_y , and H_z . By choosing $H_0 \approx 0$ and a small d_0 , the function $\psi(x, y, z) \neq 0$ only if $H_i \approx H_0$ for each i . The three dimensional (3D) nulls are then the points where the three isosurfaces $H_x = H_0, H_y = H_0, H_z = H_0$ intersect. It should be noted that at the immediate vicinity of a 3D null all the three components of magnetic field is nonzero. Similarly, a two dimensional (2D) null in a 3D coordinate space can be described as a line of intersection between H_0 isosurfaces of two nonzero magnetic field components while the third component is trivially zero at this line. Using the above technique, in Figure 1(a) we have depicted both 3D and 2D nulls of \mathbf{H} for parameters $H_0 = 0.01$ and $d_0 = 0.05$.

In Figure 1(b), we have plotted magnetic field lines about a pair of 3D nulls along with their spine axes and overlapping fan structures. From equations (15), it can easily be seen that $H_x = H_y = H_z = 0$ at $x = z = \pi$ rendering the corresponding $y = 0$ to 2π line, hereafter referred as y -line, to be a neutral line. Further insight can be gained by expanding the field components in a Taylor series in the immediate neighborhood of $x = \pi, z = \pi$ for a constant y . Retaining only the first order terms, equations (15) reduce to

$$\begin{aligned} H_x &= -(x - \pi)[\alpha_1 k^2 \sin(ky_0) + \gamma \alpha_2 l^2 \sin(l y_0)] + (z - \pi)[k^3 \cos(ky_0) + \gamma l^3 \cos(l y_0)], \\ H_y &= 0, \\ H_z &= (x - \pi)[k^3 \cos(ky_0) + \gamma l^3 \cos(l y_0)] + (z - \pi)[\alpha_1 k^2 \sin(ky_0) + \gamma \alpha_2 l^2 \sin(l y_0)]. \end{aligned} \quad (19)$$

The components H_x and H_z given by equations (19) have point antisymmetry about coordinates $x = z = \pi$ along the y -line rendering every point on it to be a X-type neutral point. It is also to be noted that only points $y = 0, \pi, 2\pi$ are rotationally symmetric about the y

line which can easily be verified by interchanging x and z . Figure 1(c) shows the magnetic configuration of one such X-type neutral point located at $y = \pi$. In addition to these 3D and 2D nulls, a set of 2D X-type neutral points in the form of shoe-shaped structures are present in \mathbf{H} as shown in Figure 1(a). These shoe-shaped nulls originate because of the superposition as can be verified by comparing Figure 1(a) with Figures 2(a) and 2(b) showing complete absence of such nulls in \mathbf{B}_1 and \mathbf{B}_2 drawn separately for $k = \{1, 1, 1\}$ and $l = \{2, 2, 2\}$. It is to be noted that the individual torsion coefficients defined by mode numbers k and l fixes the angle between the two superposing fields and also play a possible role in determining the complexity of \mathbf{H} by increasing the number of magnetic nulls.

III. NUMERICAL MODEL

A successful numerical demonstration of CS formation requires preservation of flux-freezing to an accuracy such that the identity of a fluid surface as a magnetic flux is maintained to a reasonable approximation during magnetofluid evolution. The numerical requirement is then to minimize numerical dissipation and dispersion errors which can destroy this identity. Such a minimization is a signature of a class of inherently nonlinear high-resolution transport methods that conserve field extrema along flow trajectories while ensuring higher order accuracy away from steep gradients in advective fields. For our calculations we adapt the MHD version [21] of the well established general-purpose numerical hydrodynamic model EULAG predominantly used in atmospheric and climate research [22, 23], hereafter called EULAG-MHD. The model is based entirely on the spatio-temporally second order accurate nonoscillatory forward-in-time (NFT) advection scheme MPDATA (Multidimensional positive definite advection transport algorithm) [23]. A feature unique to MPDATA and important in our calculations is its proven dissipative property mimicking the action of explicit subgrid-scale turbulence models whenever the concerned advective field is under resolved [24]. In literature, such calculations relying on the properties of nonoscillatory differencing are referred as implicit large-eddy simulations (ILES). In a recent work, Ghizaru and coworkers have successfully simulated regular solar cycles [25] while rotational torsional oscillations in a global solar dynamo has been characterized and analyzed utilizing this ILES scheme of EULAG-MHD [26]. The present understanding along with open questions on modeling the solar dynamo are summarized in reference [27].

In the following we present only the salient features of EULAG-MHD as applied to our work, whereas for details the reader is referred to Smolarkiewicz and Charbonneau [23] and references therein. We assume the flow to be solenoidal and set $\rho_0 = 1$ to fix the unit of measuring mass of the fluid elements. To solve equations (4), they are cast in the following Eulerian conservative form

$$\frac{\partial \Psi}{\partial t} + \nabla \cdot (\mathbf{v} \Psi) = \mathbf{R} , \quad (20)$$

utilizing the solenoidality of velocity \mathbf{v} and magnetic field \mathbf{B} , with $\rho_0 = 1$ and employing Cartesian coordinates. The vector $\Psi = \{v_x, v_y, v_z, B_x, B_y, B_z\}^T$ constitutes the prognosed-dependent variables while the right hand side of (20) collects all other terms along with possible forcing into a vector \mathbf{R} . The total potential pressure $\pi' = (p + B^2/2)$ and an ad hoc potential π^* added to the induction equation (3) constitute the diagnosed variables in the spirit of the hydrodynamic pressure fluctuations in the standard EULAG. An useful vector representation of this potential would be $\Phi \equiv \{\pi', \pi', \pi', \pi^*, \pi^*, \pi^*\}$. A model EULAG-MHD algorithm for integrating an inviscid version of (20) can be viewed as

$$\Psi_i^{n,\nu} = \hat{\Psi}_i + \frac{\delta t}{2} \mathbf{L} \Psi |_i^{n,\nu} + \frac{\delta t}{2} \mathbf{N}(\Psi) |_i^{n,\nu-1} - \frac{\delta t}{2} \nabla \Phi |_i^{n,\nu} , \quad (21)$$

where n, i represents discrete locations in the model (t, \mathbf{x}) domain, δt is the time increment, \mathbf{L} and \mathbf{N} are linear and nonlinear parts of the right hand side operators, and $\nu = 1, \dots, m$ numbers fixed point iterations. The only explicit element $\hat{\Psi}_i$ is given by

$$\hat{\Psi}_i = \mathcal{A}_i \left(\Psi^{n-1} + 0.5 \delta t \mathbf{R}^{n-1}, \mathbf{v}^{n-1/2} \right) , \quad (22)$$

where \mathcal{A} denotes the MPDATA advection scheme and the variable $\mathbf{v}^{n-1/2}$ is a first-order estimate of the solenoidal velocity at $t + 0.5 \delta t$. The representation (21) is then cast into a closed form

$$\Psi_i^{n,\nu} = [\mathbf{I} - 0.5 \delta t \mathbf{L}]^{-1} \left(\hat{\Psi} - 0.5 \delta t \nabla \Phi^{n,\nu} \right)_i , \quad (23)$$

where the explicit element is modified to

$$\hat{\Psi} \equiv \hat{\Psi} + 0.5 \delta t \mathbf{N}(\Psi) |^{n,\nu-1} . \quad (24)$$

All prognosed-dependent variables being spatially co-located in (23), the time updated Ψ is obtained by solving for π' and π^* two corresponding elliptic equations, implied by the solenoidality constraints (5) and (7). The numerical accuracy of viscous drag being physically inconsequential to CS formations, it is approximated to first order as $\nabla^2 \mathbf{v}^{n+1} = \nabla^2 \mathbf{v}^n + \mathcal{O}(\delta t)$, and included in the explicit counterpart $\hat{\Psi}$ of the template algorithm (24). For further discussion see [21].

The thinness of developing CSs in every numerical experiment is limited by the grid resolution. In this paper, the CSs are expected to form by progressive pressing of magnetic subvolumes with favorable magnetic morphology and eventually produce spatial scales which are smaller than the fixed grid resolution. This insufficient resolution in presence of high gradients in field variables corresponds to MPDATA in producing a locally effective residual dissipation of second order sufficient enough to maintain monotonicity of the solution, a feature well documented in literature [28]. For magnetic field this effective dissipation at locations of CS formation then results in the numerically assisted magnetic reconnection which, if localized in both space and time can mimic a physical reconnection and thereby helping to numerically identify the intermittent locations of CS formation.

IV. RESULTS AND DISCUSSIONS

Direct numerical simulations are carried out with \mathbf{H} as the initial condition. To highlight the role of unbalanced force in formation of CSs, the results are presented for two different viscosities $\mu_1 = 0.004$ and $\mu_2 = 0.0035$, with same initial magnetic field and hence Lorentz force.

To understand the overall dynamics of the magnetofluid, in Figures 3(a) and 3(b) we have plotted time evolution of the normalized average magnetic and kinetic energies for 128^3 uniform grid resolution. The solid and dashed lines correspond to viscosities $\mu_2 = 0.0035$ and $\mu_1 = 0.004$, respectively. The figures show a rise in kinetic energy at the expense of magnetic energy along with two distinct peaks in kinetic energy at $t = 6s$ and $t = 160s$ respectively while the system relaxes from the initial static state. Figures 3(c) and 3(d) illustrate the corresponding evolution of spatially averaged current density $\langle |\mathbf{J}| \rangle$ and maximum current density $|\mathbf{J}_{max}|$. Both plots show an almost symmetric sharp rise and decay about $t = 6s$ followed by an intermediate phase of quasi-steady state. A feeble second

peak is formed at $t = 160s$ which is once again nearly symmetric. The formation of such peaks in current density can generally be attributed to formation of CSs and their subsequent decay by magnetic reconnection [29]. Since in our simulations the decay of CSs is entirely due to numerically assisted reconnection, the two peaks in current density require further clarifications.

To verify numerical accuracy of the computational model, before, during and after the formation of peaks in current density, in Figures 4(a) – 4(c) we have plotted the energy budget for kinetic (dashed line), magnetic (solid line) and total (dotted line) energies (normalized to initial total energy) by calculating the numerical deviations in computed energy balance equations from their analytically correct expressions given by equations (8)-(10) for $\mu = \mu_2$. Figure 4(a) plots the numerical deviations over the whole computational time whereas Figures 4(b) and 4(c) highlight their peak values for better clarity. The plots show a maximum numerical deviation of magnitude 0.1 in magnetic energy balance from its analytically correct value of zero during formation of the first peak in current density confirming the possibility of the magnetic reconnection at $t = 6s$. After the first peak, the model regains its desired numerical accuracy, losing it again by a marginal amount during formation of the second peak in current density (Figure 4(c)). This almost accurate maintenance of energy balance in the intermediate phase along with numerically acceptable small deviations at the peaks then provides the necessary basis to assume the MPDATA generated residual magnetic diffusivity in response to under-resolved magnetic field, to be intermittent and adaptive. A seamless transition from DNS to ILES is then a possibility where the under-resolved scales are removed by this residual diffusivity and the evolution is well resolved over the whole computational time; a property of MPDATA which has already been well studied for Navier-Stokes flow of a neutral fluid [28]. The reconnection in the computational model then reasonably mimics a physical reconnection in presence of a real diffusivity.

To further understand the global dynamics, in Figure 3(e) we have plotted the magnitude of Lorentz force averaged over the computational domain. The plot shows an initial sharp rise just before the first peak in current density after which it decreases substantially. At the end of the quasi-steady state, the Lorentz force once again rises marginally before the second peak in \mathbf{J} followed by a decay. To better resolve the first peak in current density, computations are performed with varying grid resolutions. The time variations of $\langle |\mathbf{J}| \rangle$ for different uniform grid resolutions varying from 64^3 to 224^3 in steps of 32^3 , are plotted

in Figure 5(a) complemented by a plot of grid resolution vs. $|\mathbf{J}|_{max}$ in Figure 5(b). Both the plots furnish further indirect evidences of CS formation while in addition, Figure 5(b) agrees with the general understanding that the $|\mathbf{J}|_{max}$ increases with an increase in grid resolution [30, 31]. Figure 5(c) also shows a delay in appearance of the first peak in current density and hence the reconnection, with an increase in grid resolution.

From the above discussions and noting that a zero Lorentz force describes a force-free field while the simulated reconnection mimics the physical reconnection, the following picture evolves. The initial nonzero Lorentz force pushes the magnetofluid resulting in an increase in kinetic energy at the expense of magnetic energy. As the magnetofluid is pushed by the initial Lorentz force the magnetic field gradients sharpen forming CSs, till the characteristic length scale over which the magnetic field varies goes below the model resolution. The consequent reconnection then lowers the magnetic energy and hence magnitude of \mathbf{B} , while dissipation of smaller scales reduce the gradient of \mathbf{B} and hence magnitude of current density \mathbf{J} . The combined effect is that of lowering the volume averaged Lorentz force, vide Figure 3(e), which may describe an incomplete Taylor relaxation [32]. In the intermediate phase the magnetofluid evolves quasisteadily in response to this small Lorentz force. At $t = 160s$ the second peak is formed, once again through CS formations and their eventual decay as is evident from the corresponding loss of numerical accuracy in the energy balance equations (vide Figure 4(c)). An important observation in this regard is the large difference in amplitude between the two peaks in spite of their common origin, i.e., the loss in model resolution. A more overt evidence of CS formation is obtained by direct volume rendering (DVR) of $|\mathbf{J}|$ (Figure 6) which depicts the initial three dimensional structure of current density to become almost two dimensional as the current density peaks and generates small scales. The formation of CSs depends significantly on viscosity as can be inferred from Figure 3(c) where the peaks in current density appear at two different times for viscosities $\mu = 0.0035$ and $\mu = 0.004$. This is in accordance with our physical expectation that with the same Lorentz force, a highly viscous plasma will take longer time than an otherwise less viscous plasma to be pushed till the smallest model resolution is achieved.

Further insight into the dynamics of these CSs are obtained by understanding evolution of magnetic fields and current densities near the two and three dimensional nulls depicted in Figure 1(a). The following analyses correspond to simulations with viscosity $\mu_0 = \mu_2$ and uniform grid resolution of 128^3 . Figure 7 plots the time sequence of magnetic field lines at

the neighborhood of a pair of 3D nulls. Each time frame is overplotted with a preselected isosurface of \mathbf{J} having a value which is 40% of $|\mathbf{J}|_{max}$ (J40) at the first peak in current density. The initial unbalanced Lorentz force pushes the magnetofluid and hence the spine axes and fan surfaces toward each other, thereby developing gradient in magnetic field at the separator. This increased gradient in magnetic field results in a growth of current density as observed at $t = 6s$ which is cotemporal with the first current density peaks in Figure 3(c). The appearance of the J40 isosurface near $t = 6s$ at the separator is a direct evidence of CS formation. The decay of CSs after $t = 6s$ is due to the reconnection as pushing of the magnetofluid is continued below the model resolution.

The collapse of shoe-shaped nulls also have significant contribution to the first peak in current density. Each point on a shoe-shaped null is an X-type neutral point while loci of such points tracing a curved line in 3D space. Figure 8 shows the evolution of a pair of shoe-shaped nulls. This pair spans along the y -axis near $x = \pi/2, z = \pi$. During evolution, CSs are developed first at the maximum curvature region of the shoe-shaped pair followed by CS formations at other regions. Most of the current density is observed to grow near the maximum curvature region, cotemporally with first peaks in current densities at $t = 6s$. Formation and decay of CSs away from the maximum curvature region of a shoe-shaped null is observed to be near $t = 16s$ and is approximately cotemporal with the second spike in numerical deviation of magnetic energy balance plotted in figure 4(b).

In Figure 9 we have illustrated the evolution of 2D nulls overplotted with the isosurface of 40% of $|\mathbf{J}|_{max}$ at the second peak in current density. The CSs for these 2D nulls are observed to be cotemporal with the second peak in current density at the neighborhood of $t = 160s$. In the following, we describe a possible physical scenario resulting in this delayed collapse. It can easily be checked that the x and z components of the initial Lorentz force is zero only in the immediate neighborhood of the $x = z = \pi$ null line. In response to this nonzero Lorentz force the magnetofluid rotates with larger angular velocity which increases in an outward direction from the y -line and deforms magnetic field lines inhomogeneously at the plane of the 2D null. This increase in rotational kinetic energy is cotemporal with the increase in average kinetic energy plotted in Figure 3(b). The curvature of magnetic field lines and hence the magnetic tension then increases locally around the null at the expense of kinetic energy of plasma motion. This increased magnetic tension then pushes back the plasma in opposite direction at the quasi-steady phase of evolution where the kinetic energy

and hence the force acting on a fluid element is almost zero. The resulting motion is the observed to-and-fro oscillations of the field lines near the 2D null depicted in Figures 9(b) and 9(c). More importantly, during each back and forth rotation a fraction of kinetic energy is dissipated via viscosity. When this kinetic energy is mostly dissipated i.e, at the onset of the quasisteady phase, the rotational oscillations cease and the X-type configuration remains with asymmetric field structure (Figure 9(d)) having different curvatures of magnetic field in adjacent quadrants. Because of this asymmetry, the imbalance in magnetic tension then pushes the magnetofluid from two opposite quadrants towards each other. Subsequently, due to the frozen-in condition, the magnetic pressure and hence field intensity increases locally at the high curvature region at each quadrant. When the field intensity becomes sufficiently strong, the optical analogy dictates the magnetic field lines to become concave toward this local maximum along with the development of an appreciable current density. Figure 9(e) depicts such concave field lines as anticipated in chapter 8 of [7]. The boundary of the overplotted ellipse traces the field lines to provide a ready reckoning of this concavity. Finally, at $t = 160s$ the X-type neutral point is squashed to two Y-type neutral points with an extended CS, shown in Figure 9(f). This squashing is more effective in our calculations since the flow is volume preserving, so that a compression along two quadrants would result in stretching of the perpendicular quadrants. Since at different constant y -planes the field lines have different orientations in the neighborhood of a null, the corresponding CS is twisted (Figure 10) and decays through the reconnection to generate the second peak in current density.

The above process of CS formation through squashing together two initially separate regions of field (two quadrants of an X-type null), producing a gap in the intervening flux surfaces (the region of exclusion marked by the ellipse) converting an X-type null to two Y-type nulls then raises the important question on the relative effects of viscosity and magnetic diffusivity in determining the thickness of the CS. The hydrodynamics of these thinning CSs has been studied analytically by solving Navier-Stokes equations in an idealized scenario of two flux surfaces approaching each other under differential kinetic pressure [7]. The minimum thickness of a CS was found to be determined by magnetic diffusivity instead of viscosity even in the case of the latter being larger in magnitude. Simulations presented in this paper do not have the scope to explore this finding because of an absence of physical resistivity, however a coarse estimation is possible. We note that the thickness of the CS formed in

Figure 9(*f*) is actually limited by the fixed grid resolution of the 128^3 computation that is otherwise well resolved. Scales at the grid resolution are dumped selectively by the residual dissipation of MPDATA [33]. This is apparent from the peaked profile of the numerical deviations in both magnetic and kinetic energy balances in the neighborhood of $t = 160s$, plotted in Figure 4(*c*). The smallest scales then are the ones below which the residual dissipation dominates and the numerical deviations in energy balance decrease. Assuming the effect of residual dissipation on kinetic and magnetic energy rates to be comparable, the observed higher value of numerical deviation in change in magnetic energy over kinetic energy makes magnetic diffusion to be more effective than its viscous counterpart as concluded in reference [7] (chapter 9). But above arguments are only qualitative and require further numerical investigation which we leave to a future work.

V. SUMMARY

The paper numerically demonstrates CS formation in an incompressible, viscous, thermally homogeneous magnetofluid with infinite electrical conductivity and periodic boundary conditions. It also emphasizes the role of an unbalanced force pushing the magnetofluid against a viscous drag in formation of CSs. Such a study is necessary since in a multitude of physical systems like solar corona, the fluid Reynolds number is much smaller than the magnetic Reynolds number and viscous effects cannot be neglected. The initial magnetic field is a superposition of two linear force-free fields and hence has possible relevance to eruptive processes in solar atmosphere driven by magnetic flux emergence. The paper presents both indirect and direct evidences for CS formations and their eventual decay by the numerically assisted reconnection mimicking physical magnetic reconnection in terms of maintaining computed energy balance to a reasonable numerical accuracy. It is observed that the time scales over which the CSs are forming is sensitive to viscosity. With other parameters and hence the force counterbalancing viscous drag kept constant, CSs develop at an earlier time for a less viscous magnetofluid as is evident from the plots of average and maximum electric current densities. These results are in general agreement with the understanding that CSs are forming through a progressive pressing of magnetic subvolumes. To understand the limitations imposed by finite grid resolutions on the formation of CSs, further computations are performed with varying grid resolutions. It is found that the maximum of average electric

current density increases almost linearly with increasing grid resolutions. This result simultaneously verifies the importance of progressive pressing of magnetic subvolumes to develop CSs as well as the grid resolutions required to achieve them in numerical computations. A higher grid resolution would delay the occurrence of the reconnection since further pressing of the magnetofluid is required for the model resolution to go below the grid resolution, resulting in formation of the current density peak at a later time compared to the same for a lesser resolution run with other parameters kept constant.

A more direct evidence for CS formation is obtained by analyzing the dynamics of magnetic field topology near the two and three dimensional magnetic nulls in the initial magnetic field \mathbf{H} . It is observed that the current density increases in the neighborhood of both three dimensional and two-dimensional nulls. For the specific initial magnetic field used in this work, the formations of CSs and their eventual decay at the neighborhood of three dimensional nulls precedes the same near the two dimensional nulls. This delay in CS formation about the two types of magnetic nulls is explained in terms of the initial Lorentz force. The only nonzero component of the initial Lorentz force at the immediate neighborhood of a 2D null is perpendicular to the plane containing the null point whereas for the 3D nulls all components of initial Lorentz force are nonzero in the immediate neighborhood. A progressive pressing of the magnetofluid in right direction then generates CSs near 3D nulls and contributes to development of the first peak in current density. In the neighborhood of 2D nulls the Lorentz force pushes the magnetofluid in a direction perpendicular to the direction favored for CS formation and hence the delay. Eventually a CS is formed by squashing of X-type nulls to two Y-type nulls through a series of complex motions along with an intermediate appearance of a concave gap, consistent with the optical analogy. A continuous extension of these 2D CS in the third direction results in a twisted current sheet, the decay of which gives the second peak in current density.

Overall, the simulations presented in this paper are suggestive of CS formation through progressive pressing of magnetic subvolumes where the initial magnetic field is a superposition of two linear force-free fields; but with a caveat. The formation of CSs observed in this paper depends strongly on the initial magnetic field or more precisely to the existence of magnetic nulls in the initial state. The CSs are seen to develop near these nulls only, the presence of which is automatically guaranteed in an initially triply periodic magnetic field. A more realistic simulation would involve a nonperiodic boundary which is left as a future

VI. ACKNOWLEDGEMENTS

We thank the anonymous referee for providing insightful suggestions and comments to improve quality of the paper. The computations are performed using the High performance Computing (HPC) cluster at Physical Research Laboratory, India. We also wish to acknowledge the visualisation software VAPOR (www.vapor.ucar.edu), for generating relevant graphics. One of us (PKS) is supported by funding received from the European Research Council under the European Union's Seventh Framework Programme (FP7/2012/ERC Grant agreement no. 320375).

-
- [1] R. Bhattacharyya, B.C. Low, and P.K. Smolarkiewicz, *Phys. Plasmas* **17**, 112901 (2010).
 - [2] M. J. Aschwanden, *Physics of the Solar Corona* (Springer, Berlin, 2004).
 - [3] Dinesh Kumar and R. Bhattacharyya, *Phys. Plasmas* **18**, 084506 (2011).
 - [4] E. N. Parker, *Geophys. Astrophys. Fluid Dyn.* **45**, 169 (1989).
 - [5] E. N. Parker, *Geophys. Astrophys. Fluid Dyn.* **46**, 105 (1989).
 - [6] E. N. Parker, *Geophys. Astrophys. Fluid Dyn.* **50**, 229 (1990).
 - [7] E. N. Parker, *Spontaneous current sheets formation in magnetic fields* (Oxford University Press, New York, 1994).
 - [8] B. C. Low, *Astrophys. J.* **649**, 1064 (2006).
 - [9] D. P. Stern, *J. Geophys. Res.* **72**, 3995 (1967).
 - [10] D. P. Stern, *Am. J. Phys.* **38**, 494 (1970).
 - [11] D. Biskamp, *Magnetic Reconnection in Plasmas* (Cambridge Univ. Press, New York, 2000).
 - [12] E. N. Parker, *Astronophys.* **174**, 499 (1972).
 - [13] E. N. Parker, *Astrophys. J.* **330**, 474 (1988).
 - [14] E. N. Parker, *Plasma Phys. Control. Fusion* **54**, 124028 (2012).
 - [15] A. M. Janse, B. C. Low, and E. N. Parker, *Phys. Plasmas* **17**, 092901 (2010)
 - [16] B. C. Low, *Astrophys. J.* **718**, 717 (2010).

- [17] B. Ravindra, P. Venkatakrishnan, Sanjiv Kumar Tiwari, and R. Bhattacharyya, *Astrophys. J.* **740**, 637 (2011).
- [18] E. R. Priest and T. G. Forbes, *Magnetic Reconnection: MHD Theory and Applications* (Cambridge Univ. Press, New York, 2000).
- [19] Priest, E. R., and V. S. Titov, Magnetic reconnection at three- dimensional null points, *Phil. Trans. R. Soc. Lond.* **354**, 2951 (1996).
- [20] E. R. Priest and P. Demoulin, *J. Geophys. Res.* **100**, 23443 (1995).
- [21] P. K. Smolarkiewicz and P. Charbonneau, *J. Comput. Phys.* **236**, 608 (2013).
- [22] J. M. Prusa, P. K. Smolarkiewicz, and A. A. Wyszogrodzki, *Comput. Fluids* **37**, 1193 (2008).
- [23] P. K. Smolarkiewicz, *Int. J. Numer. Methods Fluids* **50**, 1123 (2006).
- [24] L. G. Margolin, W. J. Rider, and F. F. Grinstein, *J. Turbul.* **7**, N15 (2006).
- [25] M. Ghizaru, P. Charbonneau, P. K. Smolarkiewicz, *Astrophys. J. Lett.* **715**, L133 (2010).
- [26] P. Beaudoin, P. Charbonneau, E. Racine, P.K. Smolarkiewicz, *Sol. Phys.* **282**, 335 (2013).
- [27] P. Charbonneau and P. K. Smolarkiewicz, *Science*, **340**, 42, 2013.
- [28] L. G. Margolin, P. K. Smolarkiewicz, and A. A. Wyszogradzki, *J. Appl. Mech.* **73**, 469 (2006).
- [29] R. M. Kerr and A. Brandenburg, *Phys. Rev. Lett.* **83**, 1155 (1999).
- [30] I. J. D. Craig and Y. E. Litvinenko, *Phys. Plasmas* **12**, 112105 (2005).
- [31] C. Mellor, C. L. Gerrard, K. Galsgaard, A. W. Hood, and E. R. Priest, *Sol. Phys.* **227**, 39 (2005).
- [32] J. B. Taylor, *Phys. Rev. Lett.* **33**, 1139 (1974).
- [33] A. Domaradzki, Z. Xiao, and P. K. Smolarkiewicz, *Phys. Fluids* **15**, 3890 (2003).

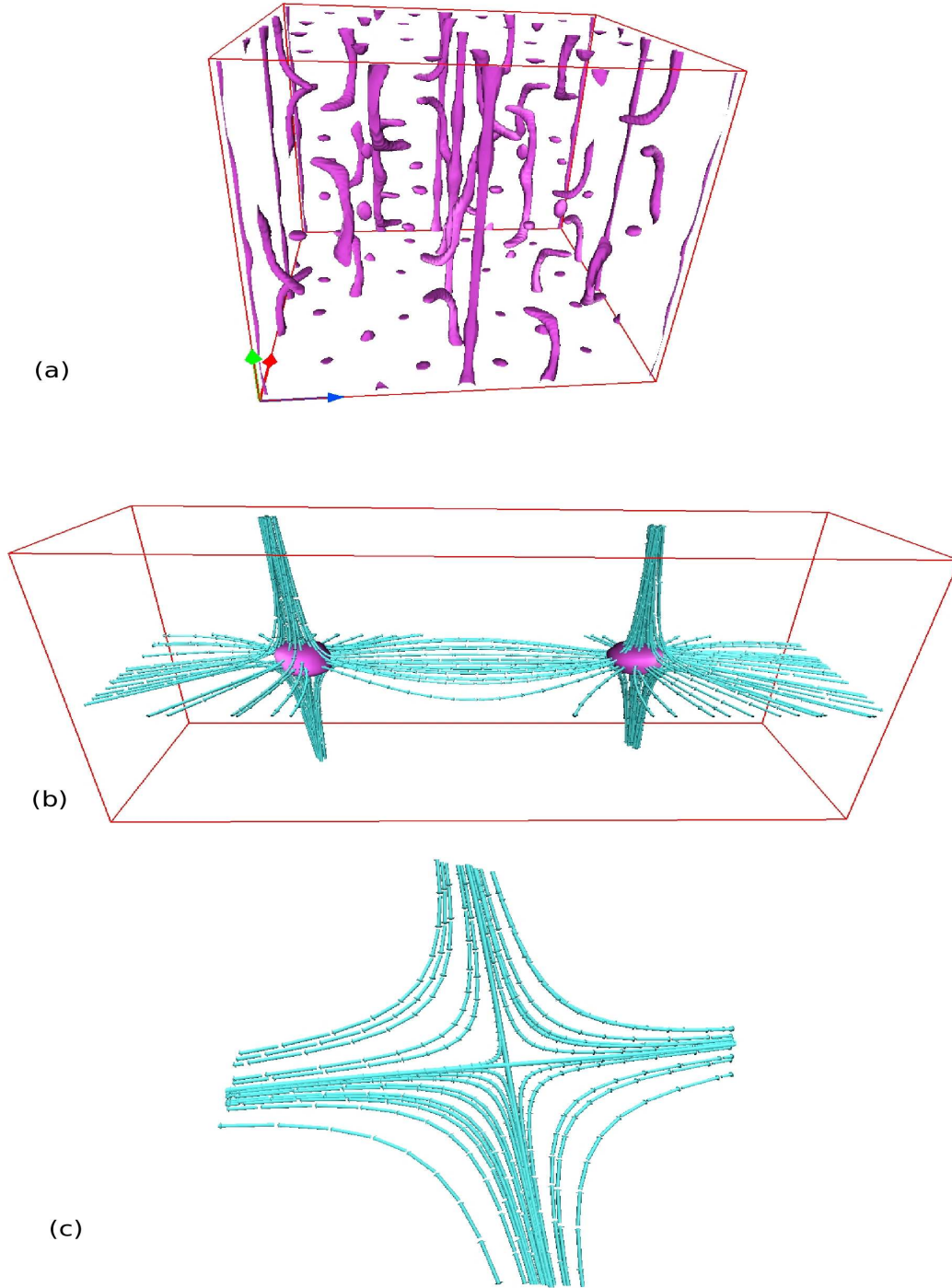


FIG. 1: (color online). Figure (a) shows magnetic nulls represented by isosurfaces of \mathbf{H} with parameters $H_0 = 0.01$ and $d_0 = 0.05$ for $k = \{1, 1, 1\}, l = \{2, 2, 2\}$ and $\gamma = 0.5$. A pair of 3D nulls with corresponding spine axes and fan planes are shown in Figure (b). The field topology along with separatrices near the 2D null located at $x = \pi, y = 3\pi/2, z = \pi$ is depicted in Figure (c) which is of X-type geometry.

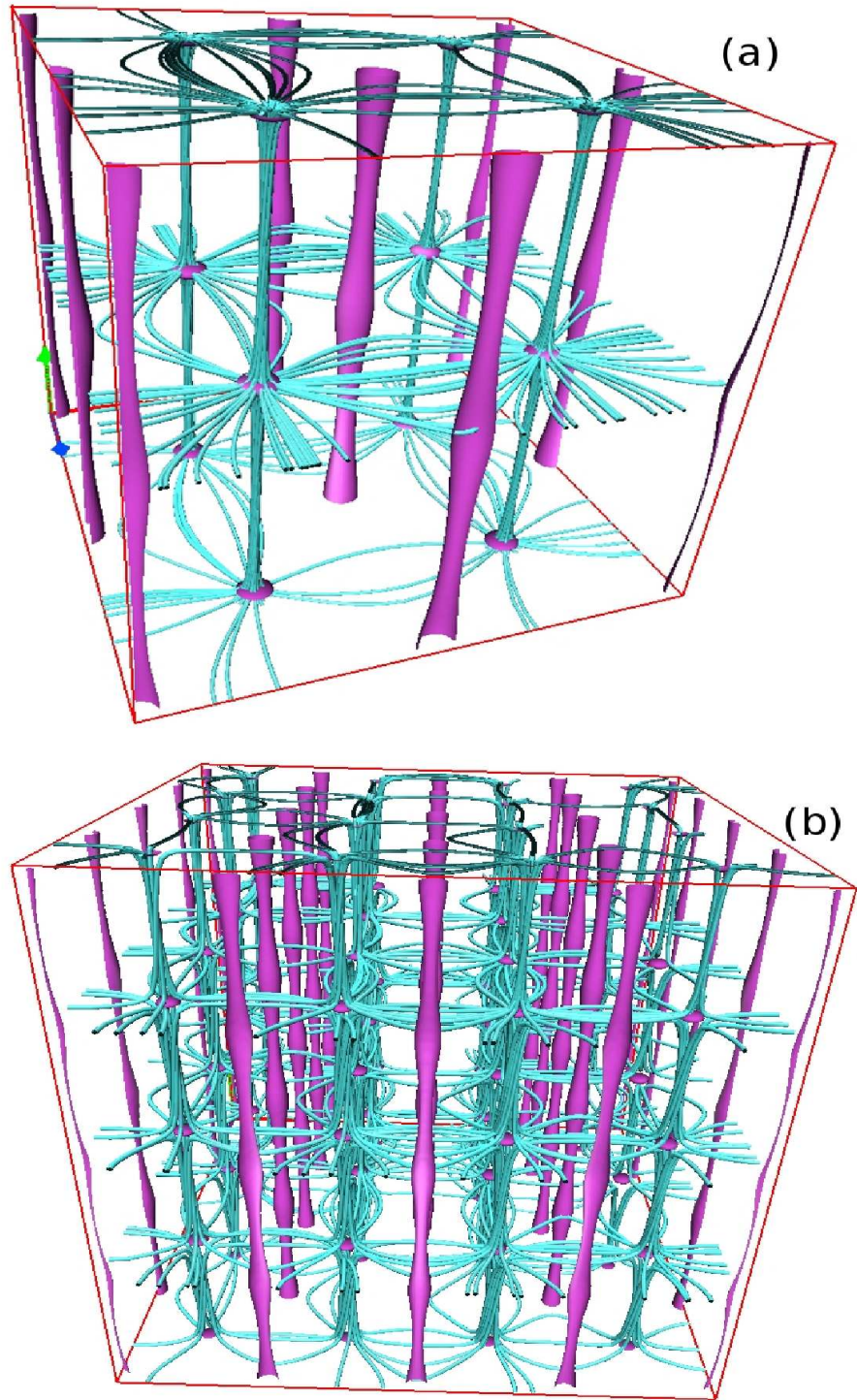


FIG. 2: (Color online). Figures (a) and (b) depict the magnetic nulls represented by isosurfaces with parameters $H_0 = 0.01$ and $d_0 = 0.05$ of force-free magnetic fields \mathbf{B}_1 and \mathbf{B}_2 separately. The connectivity of field lines in the neighborhood of these nulls are shown by solid lines.

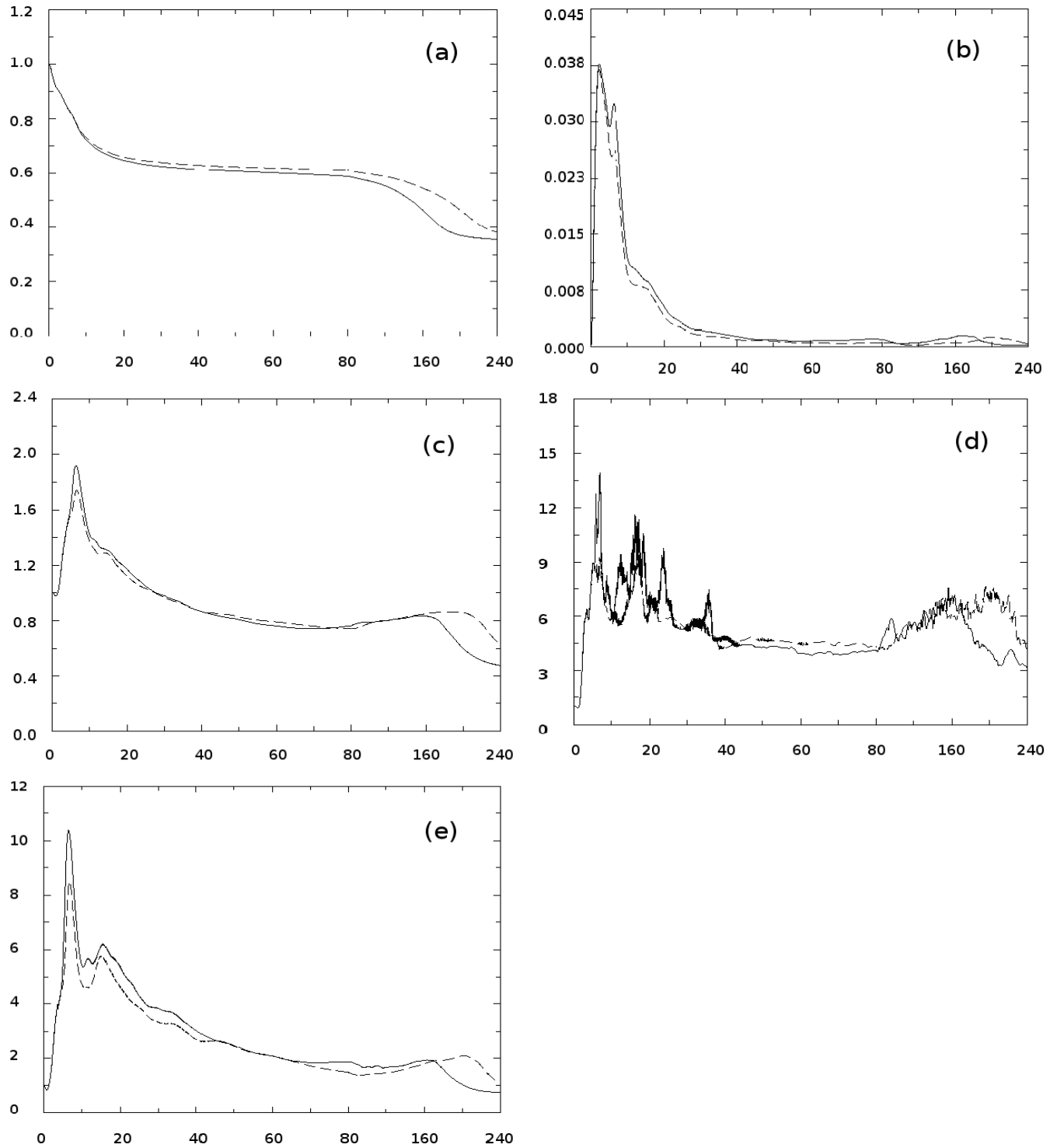


FIG. 3: History of (a) magnetic energy, (b) kinetic energy, (c) $\langle |\mathbf{J}| \rangle$, (d) $|\mathbf{J}_{max}|$, (e) grid averaged Lorentz force, for viscosities $\mu_1 = 0.0035$ (solid lines) and $\mu_2 = 0.004$ (dashed lines). For better clarity in representing the peaks, the time axis is morphed to $t' = s_0 t$ with $s_0 = 4$ from $t = 0s$ to $t = 80s$ and $s_0 = 1$ for $t > 80s$ to $t = 240s$

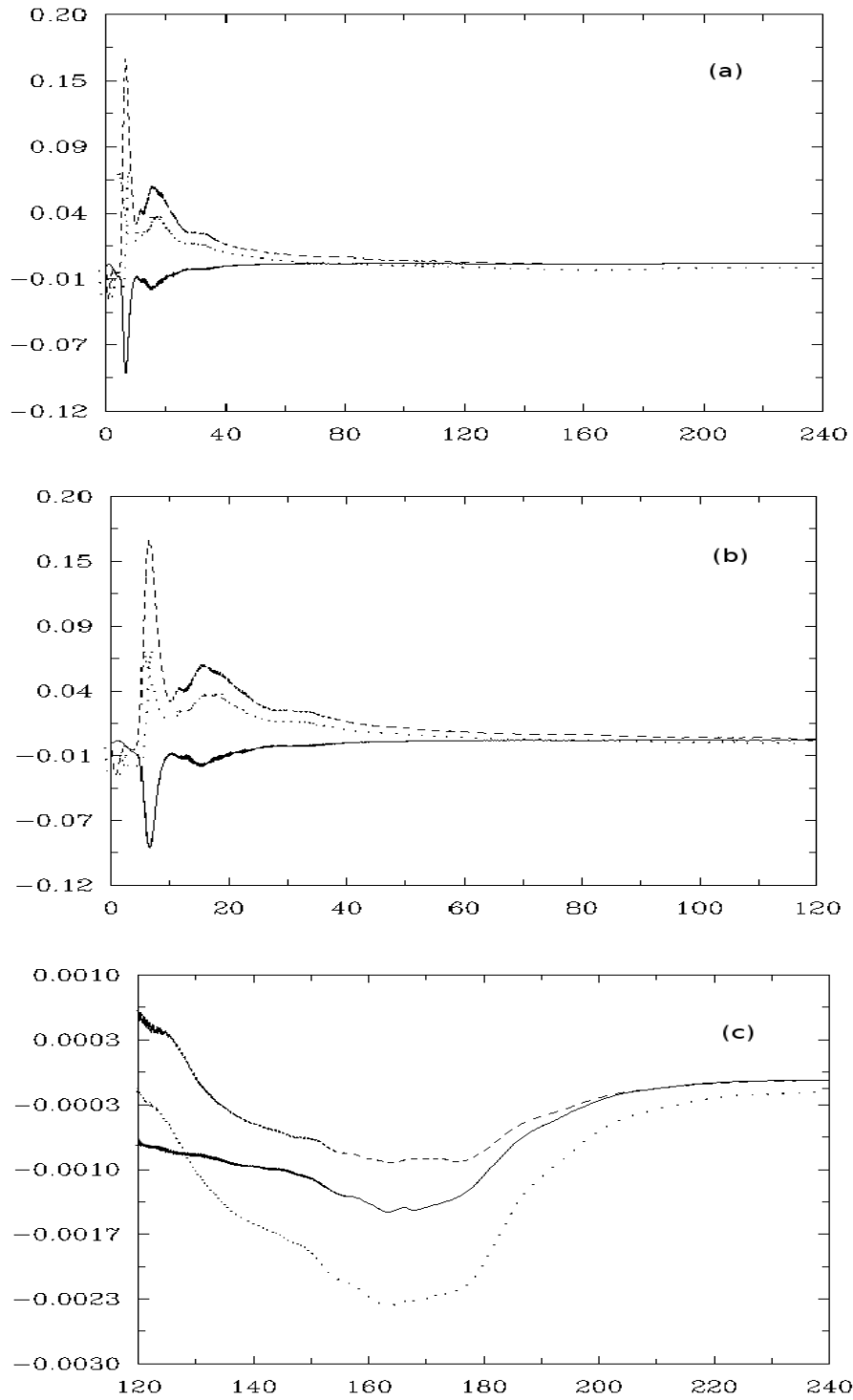


FIG. 4: History of energy budget for total (dotted line), kinetic (dashed), and magnetic (solid) energies for viscosity $\mu_1 = 0.0035$, drawn for full computational domain (4(a)) and localized at the two peaks of current density (4(b) and 4(c)).

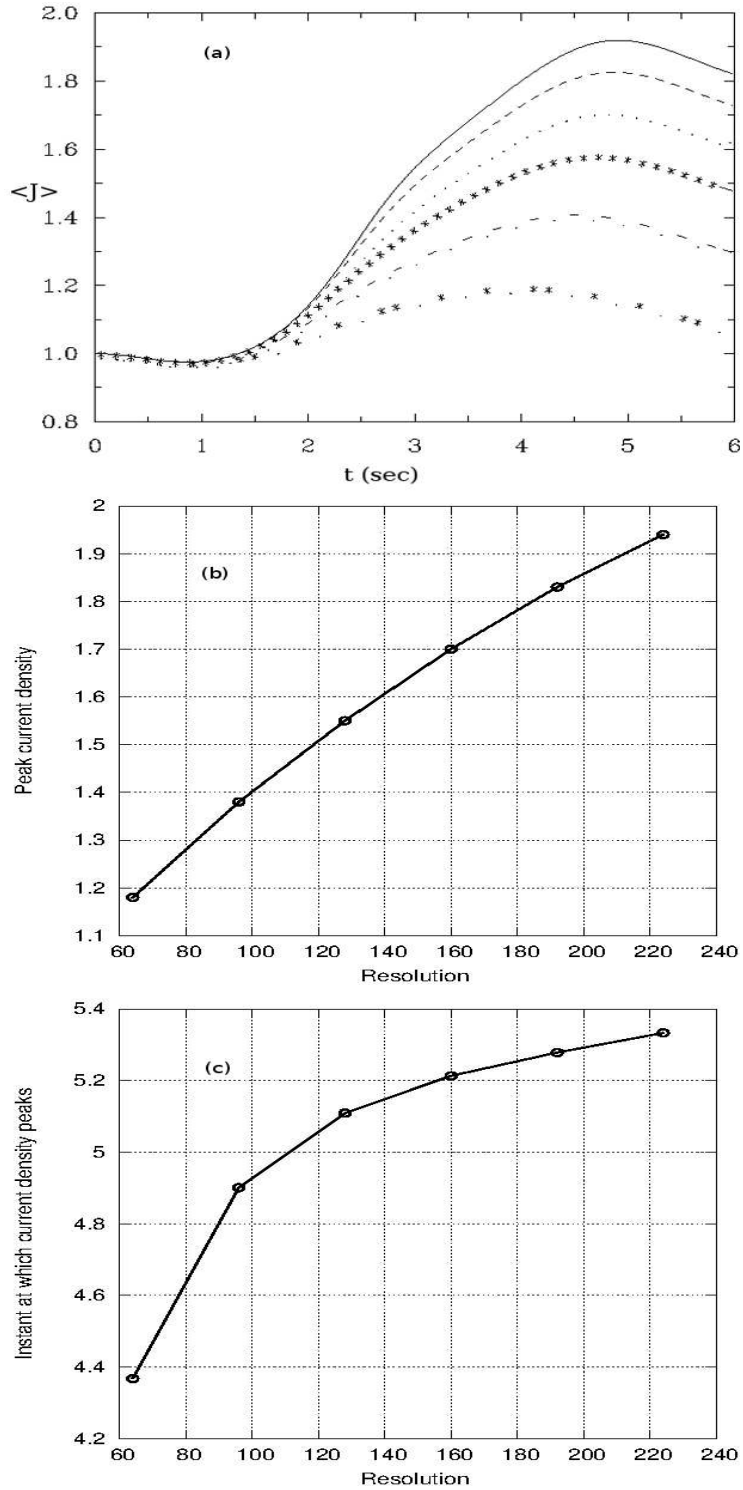


FIG. 5: Figure (a) depicts the evolution of current densities averaged over the computational volume, for different grid resolutions varying from 64^3 to 224^3 in steps of 32^3 . Figures (b) and (c) illustrate the variations of $|\mathbf{J}_{max}|$ and the instant at which $\mathbf{J} = |\mathbf{J}_{max}|$ with increasing grid resolutions. The plots are in agreement with the general expectation that an increase in grid resolution would delay the formation of peaks in current density while increasing their amplitudes.

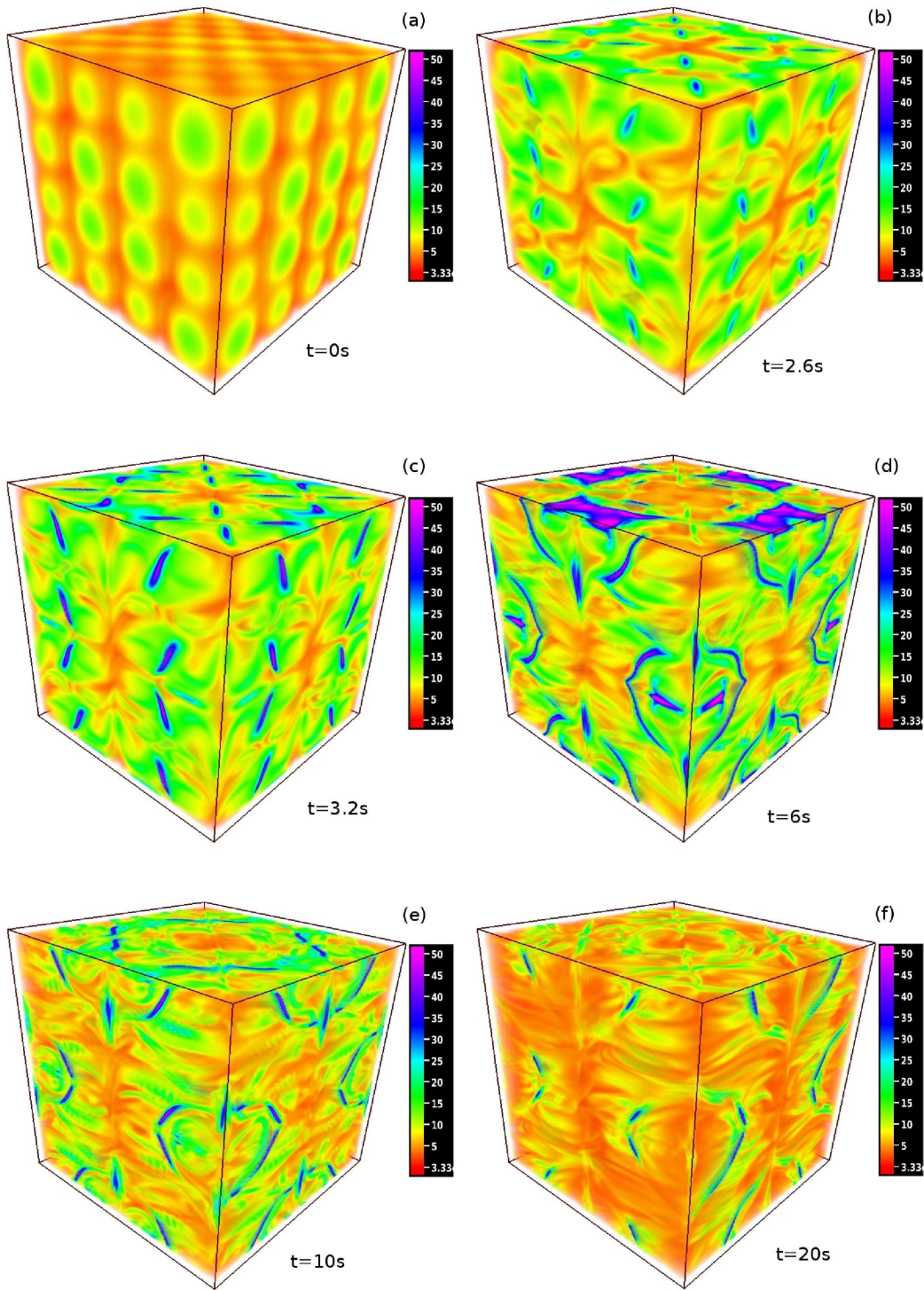


FIG. 6: (Color online). Time sequence of direct volume rendering of $\langle |\mathbf{J}| \rangle$ for 128^3 uniform grid and viscosity $\mu = 0.0035$, showing growth and decay of the current density.

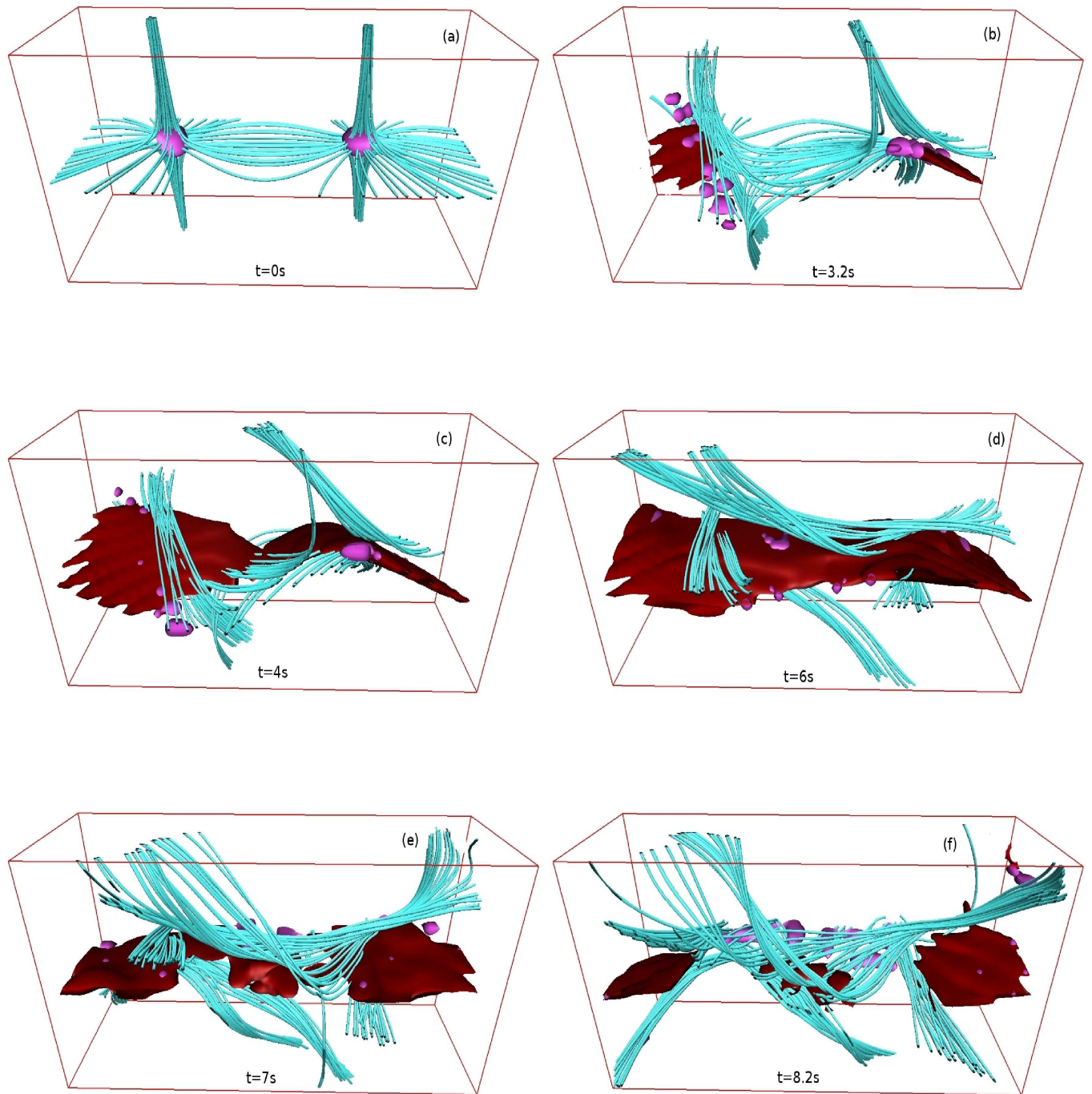


FIG. 7: (Color online). Time evolution of 3D magnetic nulls and corresponding spine and fan surfaces, overlapped with isosurface (in red) of current density having a magnitude of 40% of its peak value highlighting the locations where current sheets are forming.

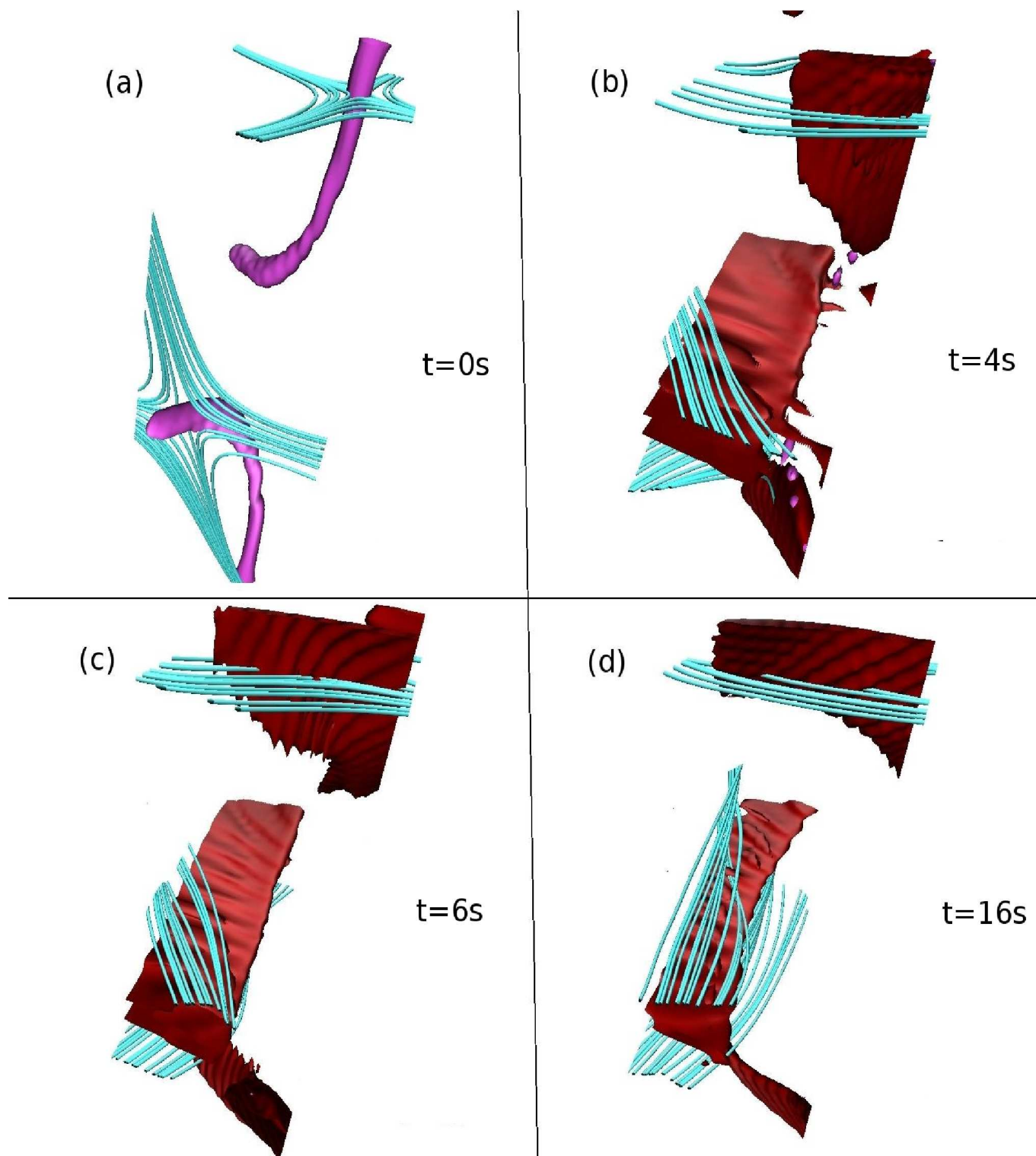


FIG. 8: (Color online). History of a pair of adjacent shoe-shaped magnetic nulls and neighbouring magnetic field lines, overplotted with the same isosurface as in Figure 7 to visualize current sheet formations. The viscosity and grid resolutions are $\mu = 0.0035$ and 128^3 respectively.

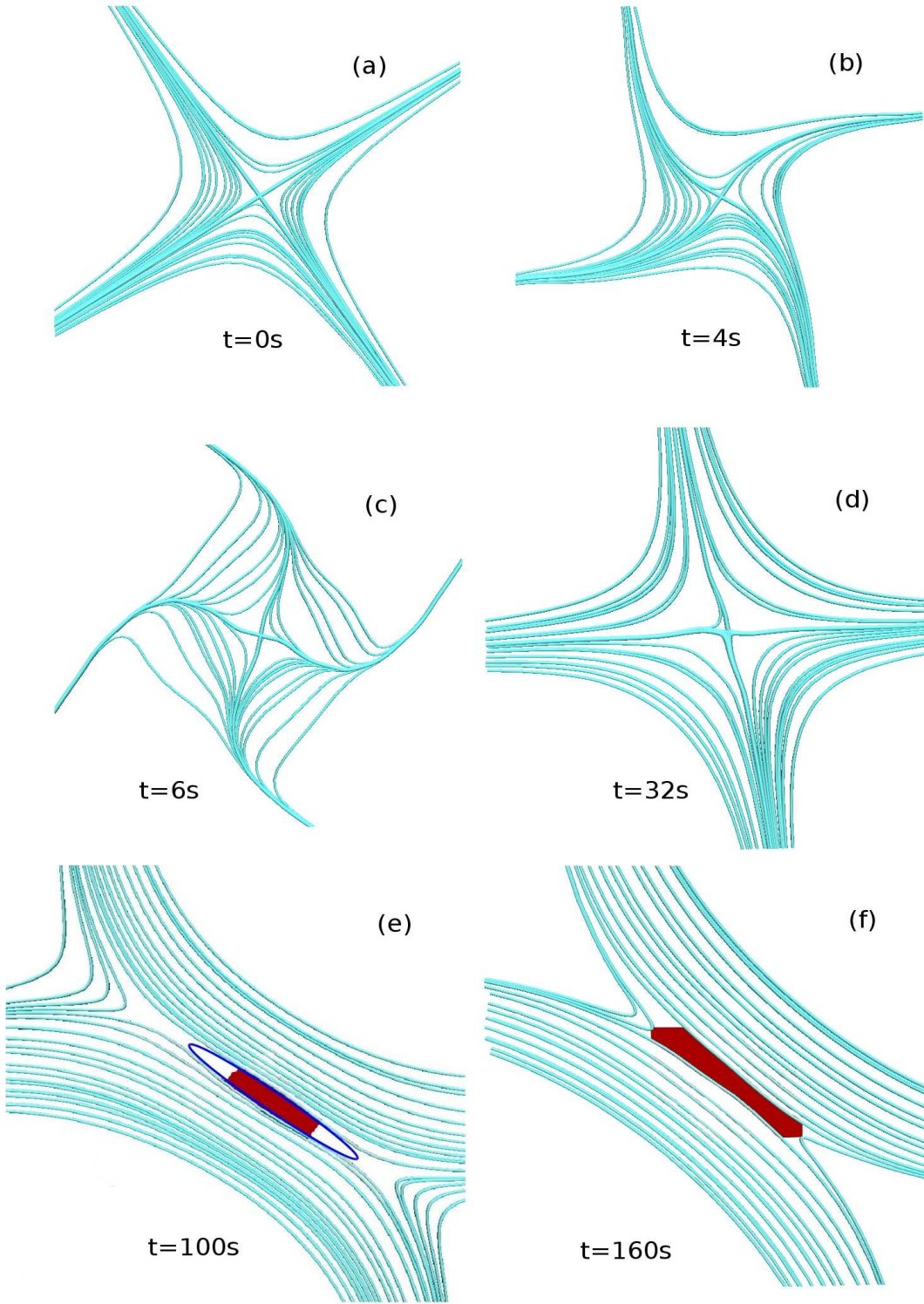


FIG. 9: (Color online). Figures (a) – (f) illustrate the time evolution of a representative 2D magnetic null located at $x = \pi, y = 3\pi/2, z = \pi$ and null fields overplotted with isosurfaces (in red) of 40% of $|\mathbf{J}|_{max}$ at the second peak in current density, appearance of which at $t=160s$ confirms the formation of current sheet at the Y-type null.

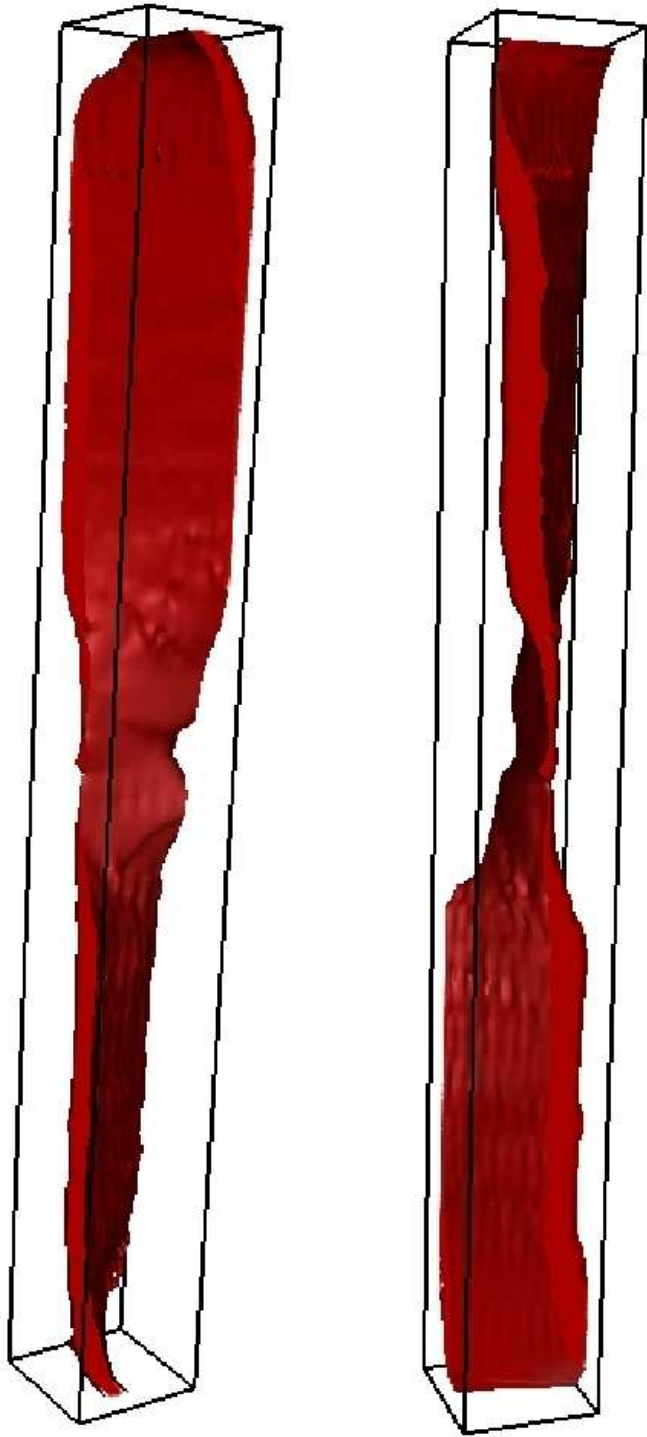


FIG. 10: (Color online). Current sheet along y and $x = z = \pi$ at $t = 160s$ represented by the same isosurface of current density as in Figure 9, plotted for two different viewing angles to emphasize its twisted nature.